

RESEARCH ARTICLE

Mechanical responses of rat vibrissae to airflow

Yan S. W. Yu¹, Matthew M. Graff¹ and Mitra J. Z. Hartmann^{1,2,*}

ABSTRACT

The survival of many animals depends in part on their ability to sense the flow of the surrounding fluid medium. To date, however, little is known about how terrestrial mammals sense airflow direction or speed. The present work analyzes the mechanical response of isolated rat macrovibrissae (whiskers) to airflow to assess their viability as flow sensors. Results show that the whisker bends primarily in the direction of airflow and vibrates around a new average position at frequencies related to its resonant modes. The bending direction is not affected by airflow speed or by geometric properties of the whisker. In contrast, the bending magnitude increases strongly with airflow speed and with the ratio of the whisker's arc length to base diameter. To a much smaller degree, the bending magnitude also varies with the orientation of the whisker's intrinsic curvature relative to the direction of airflow. These results are used to predict the mechanical responses of vibrissae to airflow across the entire array, and to show that the rat could actively adjust the airflow data that the vibrissae acquire by changing the orientation of its whiskers. We suggest that, like the whiskers of pinnipeds, the macrovibrissae of terrestrial mammals are multimodal sensors – able to sense both airflow and touch – and that they may play a particularly important role in anemotaxis.

KEY WORDS: Whisker, Trigeminal, Flow-sensing, Wind, Anemotaxis, Anemotactic behavior, Wind following

INTRODUCTION

With the exception of a few species, the faces of therian mammals are covered in vibrissae (whiskers), typically arranged on the cheek in an orderly pattern of rows and columns (Brecht et al., 1997; Muchlinski, 2010; Grant et al., 2013a). Whiskers have been the subject of research in both rodents (Bosman et al., 2011) and marine mammals (Dehnhardt et al., 2001; Hanke et al., 2013), but studies in these animals have largely focused on separate aspects of whisker function.

Rodents exhibit 'whisking' behavior, in which the vibrissae are rhythmically (5–25 Hz) tapped and brushed against surfaces to enable direct tactile exploration (Welker, 1964; Carvell and Simons, 1990). Studies in rodents have therefore focused primarily on the use of whiskers as contact sensors, investigating questions in active tactile perception and sensorimotor integration (Diamond et al., 2008).

In contrast to rodents, pinnipeds do not exhibit clear whisking behavior, although the entire mystacial pad can move slightly as a whole. Studies in pinnipeds have focused primarily on the use of whiskers as remote flow sensors (Gläser et al., 2011; Miersch et al., 2011; Wieskotten et al., 2011). For example, it has been shown that

seals can use their whiskers to track the wake of an artificial fish (Dehnhardt et al., 2001).

To date, however, few if any studies have investigated the possibility that terrestrial mammals might also use their vibrissae as flow sensors. If air currents of the magnitude typically found in natural environments generate significant vibrissal motion, then animals may exploit this sensation to their advantage.

This study takes the first steps towards investigating the possibility that the vibrissae may serve as airflow sensors in terrestrial mammals. We focus specifically on characterizing the mechanical response of the rat's 'macrovibrissae' to airflow. The rat's macrovibrissae range in length between ~1 and 6 cm, much longer than the numerous 'microvibrissae' (~1 mm), which segue into the fur (Welker, 1964; Brecht et al., 1997; Hartmann, 2001; Kuruppath et al., 2014).

We first quantify how individual macrovibrissae bend and vibrate in response to airflow, and then generalize these results to predict how these responses will vary across the entire vibrissal array. Results are discussed in the context of a potential functional role for vibrissae in anemotactic behavior and in view of the large body of literature on flow sensing in arthropods (Grasso and Basil, 2002; Humphrey and Barth, 2007; Casas and Dangles, 2010; Reidenbach and Koehl, 2011; Keil, 2012).

MATERIALS AND METHODS

All procedures were approved in advance by Northwestern's Animal Care and Use Committee.

Experimental setup

The experimental setup illustrated in Fig. 1A allowed us to independently vary airflow speed and the orientation of the vibrissa's intrinsic curvature relative to the airflow.

Individual whiskers were plucked from one 2-year-old, female Long-Evans rat [*Rattus norvegicus* (Berkenhout 1769)] and rigidly clamped to a metal post. No more than 96 h elapsed between the time that the whisker was plucked and the time that the experiment began.

Two high-speed video cameras (Photron, FASTCAM-1024PCI), each fitted with a macro lens (Nikon, AF Micro-Nikkor 60 mm f/2.8D), were mounted orthogonally ~35 cm from the whisker. The F-stop was set to F16 and 8-bit monochrome images were obtained with 1024×1024 pixel resolution at 1000 frames s⁻¹. Resolution near the focal plane in the top and front camera views was 14.4±0.5 and 15.2±0.8 pixels mm⁻¹, respectively. A command-obey configuration and software trigger provided synchronization (±12.7 nS per the manufacturer's specifications).

Orientation of the whisker relative to the airflow and quantification of airflow speed

The present experiments aimed to study the quasi-static deflection (bending) and vibrations of the whisker in response to naturalistic airflow stimuli rather than the flow structure around the whisker. Therefore, no effort was made to ensure flow laminarity or to characterize the details of the flow structure. We did, however,

¹Department of Mechanical Engineering, Northwestern University, Evanston, IL 60208, USA. ²Department of Biomedical Engineering, Northwestern University, Evanston, IL 60208, USA.

*Author for correspondence (hartmann@northwestern.edu)

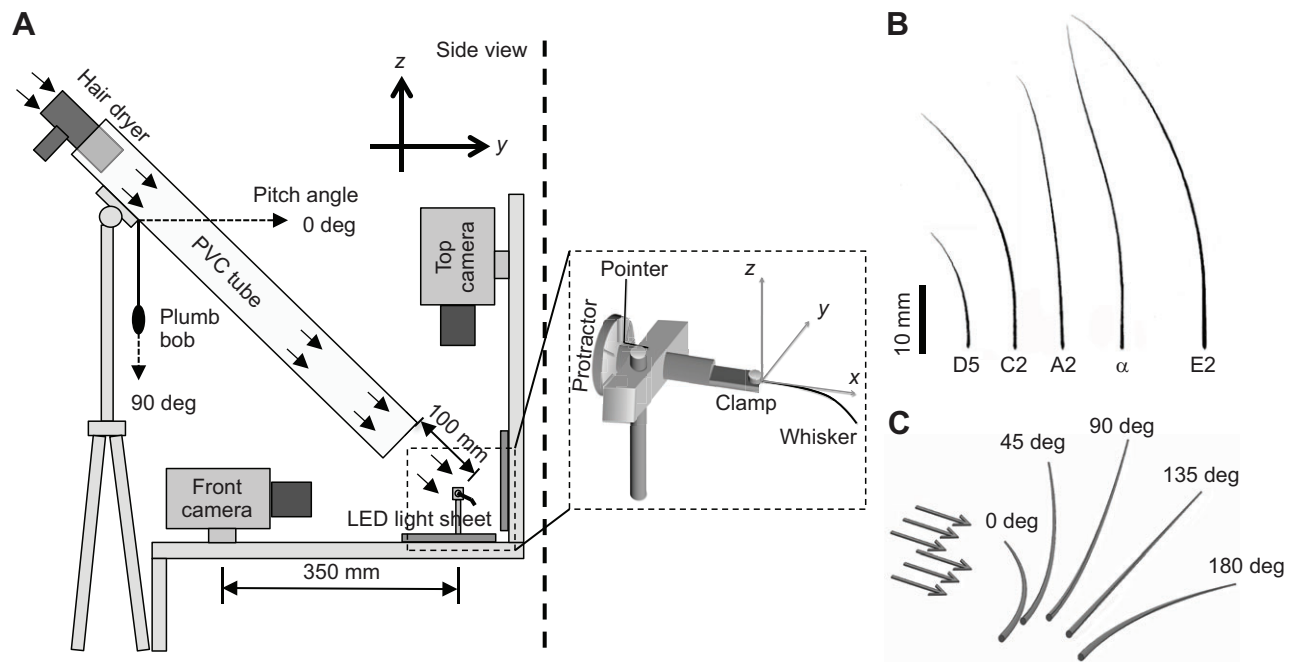


Fig. 1. The experimental setup allowed airflow speed and the orientation of the rat vibrissa's intrinsic curvature relative to the airflow to be varied independently. (A) Schematic of the setup and definition of coordinate systems. The x -axis is directed axially, along the length of the whisker near its base, the y -axis is transverse to the whisker and parallel to the ground, and the z -axis is transverse to the whisker, vertical. The air source was fixed in position at a 45 deg angle relative to the ground. The expanded and rotated view illustrates the whisker mounted on the post along with the protractor used to determine the orientation angle of the whisker's intrinsic curvature relative to the airflow. Two LED light sheets provided illumination. (B) Manual tracings of the scans of the five whiskers used in the present experiment. (C) Definition of the orientation angle of the whisker relative to the airflow. A protractor was used to orient the whisker relative to the airflow. Five orientation angles (0, 45, 90, 135 and 180 deg) were tested. When in the 0 and 180 deg orientations, the plane of the whisker was in the plane of the airflow. When oriented at 90 deg, the plane of the whisker was perpendicular to the plane of the airflow.

choose airflow speeds that the rat might encounter in the natural environment. Meteorological studies find typical land–surface wind speeds between 0 and 5 m s^{-1} (Monahan et al., 2011). We confirmed this range using a hot wire anemometer (Omega, model HHF42, resolution $\pm 0.1 \text{ m s}^{-1}$) to measure airflow speeds in locations where rats are expected (bushes, dumpsters, fields, etc.). Although these measurements were not comprehensive, they ensured that our range was reasonable, even for airflow close to objects or the ground.

A hair dryer without heating was fixed in position to blow air at the whiskers through a PVC tube 4 inches (10.16 cm) in diameter and 38 inches (96.52 cm) long. The PVC tube was oriented 45 deg relative to the ground to avoid obstructing the cameras.

The hair dryer had two speed settings. A variable diameter air constrictor was placed over the intake to obtain a total of six airflow speeds (approximately 0.5, 1.4, 2.2, 3.4, 4.4 and 5.6 m s^{-1}). The anemometer was used to measure the average airflow speed at the whisker. At the lowest speed setting, the speed measured at the whisker tip and base were the same, within the anemometer's resolution. At the highest speeds, the speed at the tip and base differed by at most 0.2 m s^{-1} . For these trials, the average speed at the tip and base was taken to be the speed around the whisker.

Fig. 1B illustrates the shapes and lengths of the five whiskers used in the experiments. From shortest to longest, the whiskers were D5, C2, A2, α and E2. Whisker parameters are listed in Table 1.

Table 1. Geometric parameters of the whiskers and values of the characteristic coefficients (λ_j) used to predict resonant frequencies for the fixed-free conical beam

Whisker identity	Length (mm)	Tip diameter (μm)	Base diameter (μm)	$(A_t/A_b)^{1/2}$	λ_j for Mode 1	λ_j for Mode 2	λ_j for Mode 3
				1.00	3.52	22.03	61.70
				0.50	4.63	19.55	48.50
				0.33	5.29	18.76	43.78
				0.25	5.85	18.51	41.34
A2	36.5	14	127	0.11	7.09	18.69	37.44
α	43.1	13	127	0.10	7.16	18.71	37.22
				0.10	7.20	18.71	37.10
E2	49.6	14	174	0.08	7.46	19.12	37.33
C2	34.3	11	149	0.07	7.63	19.39	37.45
D5	17.2	2	130	0.01	8.55	20.87	38.30
				0	8.72	21.15	38.45

Values in cells with a white background are taken directly from table 1 of Georgian (1965). Values for the vibrissae used in the present study are in cells shaded with a gray background. These values were interpolated from the data of Georgian (1965) to adjust for measured tip and base diameter. A_t is the area of the tip of the conical cantilever beam and A_b is the area of the base.

As seen in Fig. 1B, rat vibrissae have an intrinsic curvature that approximates a parabola (Knutsen et al., 2008; Towal et al., 2011; Quist and Hartmann, 2012). Each whisker was aligned with a protractor to obtain five different orientations relative to the airflow (Fig. 1C), and the six airflow speeds were tested at each orientation.

Tracking the whisker's three-dimensional shape

The two-dimensional (2D) camera views were tracked semi-automatically. In the first frame of each trial, the user manually selected the whisker's base point in top and side views. Because the base was clamped, its location was assumed constant throughout a trial. The tracking algorithm worked from base to tip, finding the darkest pixels along the whisker's length.

Three-dimensional (3D) merging of the 2D images was performed using the Camera Calibration Toolbox for MATLAB (Bouquet, 2013) using a 6×6 calibration grid. Each grid element was 5.08 mm (0.2 inches) square. Images of the calibration pattern were taken at 16 unique orientations spanning the range of the whisker's movement. The toolbox uses these images to create a model for each camera, including corrections for lens distortion. The models allowed us to merge conjugate pairs of points in the two camera views to a single 3D point. Conversely, we were also able to guess a 3D location and project the point into each camera view.

Because we could not place fiducial markers on the whisker without changing its dynamics, we solved the inverse problem, in which we guessed the 3D position of a whisker node and fit its projections in the 2D images using an optimization algorithm. The optimization begins at the whisker base because it provides one conjugate pair from which to start.

The optimization divided the whisker into nodes 2 mm apart, numbered from 1 to N from base to tip. The optimization used rigid body transformations to rotate node $n+1$ about node n . It used gradient descent to minimize the distance between each guess (of the position of the 3D node) and the closest tracked point in each 2D projection image. Each node's optimization was deemed complete when the spatial tolerance (change in total error between the 3D-back-projected and two actual 2D views) was less than 1×10^{-4} mm or a maximum of 1000 iterations was reached. As a result of blurring around the tip, whiskers were tracked to ~80% of the total arc length.

Quantifying whisker mass, length, diameter, volume, density and taper

Whiskers were massed using a Mettler-Toledo UMX2 ultra microbalance ($\pm 0.1 \mu\text{g}$). After massing, the whiskers were scanned on a flatbed scanner (Epson Perfection 4180 Photo) and traced in Photoshop (Fig. 1B).

Next, we applied correction fluid (white-out) to add ~5 mm stripes to each whisker in ~2 mm intervals. The diameter of the whisker at each stripe transition was measured at magnifications between 10× and 40× under an Olympus BX60 microscope. Photos were taken with an MBF Bioscience DV-47 camera. The arc length of each striped/non-striped segment was obtained by re-scanning on the flatbed scanner.

Each whisker segment was approximated as a truncated cone. The whisker's total volume was obtained by summing the segmental volumes. Density was calculated by dividing the whisker's mass by its volume. Taper was determined by performing a parabolic fit to the diameters measured at the locations of the stripe transitions along the whisker. Base and tip diameters were obtained from the parabolic fit.

Quantifying bending direction and bending magnitude

The present work was concerned with steady-state, not transient, deflections of the whisker, so video recording began at least 10 s after airflow was applied and lasted for 5 s.

The whisker base was set as the origin of a Cartesian coordinate system. As in previous work (Towal et al., 2011; Quist et al., 2014; Huet et al., 2015), the x -axis was defined to lie along the proximal portion of the whisker (Fig. 1A, inset).

We defined the position of each node n with the whisker at rest as $[x_0, y_0, z_0]$. We defined the mean position (time average position) of each node n with the whisker in airflow as $[x_m, y_m, z_m]$:

$$x_m = \frac{1}{T} \sum_{k=1}^T x_k, \quad y_m = \frac{1}{T} \sum_{k=1}^T y_k, \quad z_m = \frac{1}{T} \sum_{k=1}^T z_k, \quad (1)$$

where k is the frame number (1 ms frame^{-1}), T is the video duration (5000 frames) and $[x_k, y_k, z_k]$ is the position of node n at frame k .

The tracked points on the whisker defined through Eqn 1 allowed us to define the whisker's bending direction and bending magnitude, as follows. For each node, bending direction was quantified by the angle between the direction of airflow and the vector connecting the position of the node at rest ($[x_0, y_0, z_0]$) to the mean position of the node in the airflow ($[x_m, y_m, z_m]$). For each node, bending magnitude was calculated as the angle θ between two vectors: (1) the vector connecting the base point to the position of the node at rest, and (2) the vector connecting the base point to the mean position of the node in airflow. The definition of bending magnitude is schematized in two dimensions in Fig. 2.

If the whisker were rigid, or if the follicle that held the whisker were very flexible, then the whisker would rotate only at its base, as occurs for flow-sensing insect hairs (Dechant et al., 2006). In this case, the bending magnitude would be identical at all nodes along the whisker (Fig. 2A). However, rat whiskers are flexible, so bending magnitude must be computed at each node along the whisker length (Fig. 2B).

Fig. 2 illustrates the bending magnitude θ in 2D for visual clarity; however, θ was calculated in three dimensions as the angle between two vectors. Whisker bending does not occur entirely in the bending direction because turbulence causes out-of-plane effects. However,

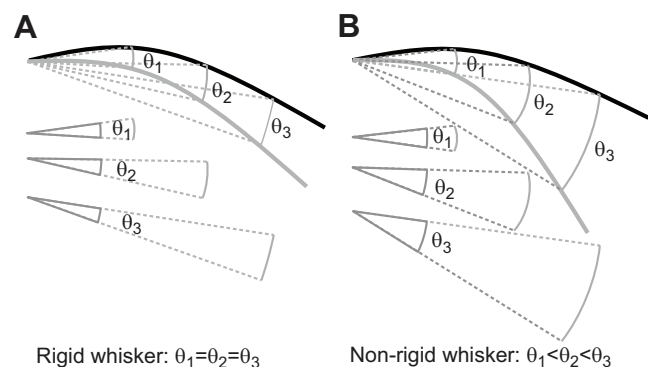


Fig. 2. Schematic of bending magnitude (θ), quantified as the angular displacement of each node from rest to its position in the presence of airflow. The black curve indicates the whisker at rest, and the gray curve indicates the mean position of the whisker in the presence of airflow. If the whisker were rigid (left schematic), then θ would be the same at each node. Because real rat whiskers are flexible, the bending magnitude θ increases from base to tip (right schematic).

the out-of-plane bending was small, with an average value of 0.0 deg (see Results).

Quantifying vibration frequency

As described in the Results, all whiskers vibrated strongly in response to airflow, but the major axis of vibration was difficult to determine. We choose to quantify vibration frequency in the y -direction (transverse to the whisker, parallel to the ground).

For each whisker, a frequency representation was obtained from the y -position data (in units of mm) from the tracked node closest to 40% from the whisker base. Each 5000 ms trial at each of the five orientations was split into five segments of 1000 ms each, for a total of 25 segments.

MATLAB™ was used to calculate the absolute value of the fast Fourier transform of each of the 25 segments of data, and these transformed signals were divided by the length of the segments. This procedure yielded 25 spectra for the y -amplitude as a function of frequency. These 25 spectra (units of mm) were then averaged, and this final average was termed the mean amplitude spectrum.

As shown in the Results, the peaks in the mean amplitude spectrum were broad, reflecting the wide range of frequencies and directions that characterized each whisker's vibrations. To associate a single experimentally measured frequency with these broad peaks, a two-step procedure was used.

First, we determined the minimum and maximum values that could reasonably be expected for each of the resonance modes of each whisker, i.e. the widest possible range of expected frequencies. To do this, we used the following equation, which describes the resonant frequency modes (f_j) for a fixed-free tapered cantilever beam (Georgian, 1965):

$$f_j = (\lambda_j D / 4S^2)(E / \rho)^{1/2} / (2\pi). \quad (2)$$

In Eqn 2, the whisker's base diameter (D) and arc length (S) are measured values, and density (ρ) was calculated from the mass and volume (see 'Quantifying whisker mass, length, diameter, volume, density and taper', above). We determined the characteristic coefficient (λ_j) from table 1 in Georgian (1965). The subscript j indicates the mode number. To determine the widest possible range of expected frequencies (f_j), we set Young's modulus (E) either to 3 or 11 GPa in Eqn 2.

Second, we found the crest of the amplitude spectrum within the range of expected frequencies. To do this, we found the points at

which the amplitude spectrum intersected the minimum ($E=3$ GPa) and maximum ($E=11$ GPa) predicted frequencies. Those two points were connected by a line. We computed the vertical distance from the line to the amplitude spectrum at each frequency. The largest distance defined the crest of the amplitude spectrum in that region, and the corresponding frequency was considered the experimentally measured resonance frequency for that mode.

RESULTS

We begin by showing that the whisker primarily bends in the direction of airflow and vibrates around a new average position. The bending magnitude is shown to depend strongly on airflow speed, orientation of the whisker relative to the airflow and whisker geometry. The vibrations occur at frequencies correlated with the whisker's resonance modes. We conclude by analyzing how bending and vibrations are likely to vary across the whisker array in response to airflow.

The whisker primarily bends in the direction of the airflow and oscillates about that new position

The base of each of five whiskers (E2, α , A2, C2 and D5) was rigidly clamped to a post, and air was directed on the whisker at different speeds. All results are described in the experimental reference frame in which the direction of airflow is taken to be 0 deg, the z -axis is vertical, the y -axis is parallel to the ground, and the x -axis is parallel with the whisker base.

The typical response of a whisker to airflow of moderate speed (2.3 m s^{-1}) is shown in Fig. 3, with the whisker oriented 45 deg relative to the airflow. This figure quantifies the motions of the same whisker shown in Movie 1.

Three characteristics of the whisker's response are seen in Fig. 3. First, the whisker bends to a new mean position under the influence of the airflow, and it oscillates about that new mean. In Fig. 3A, the vibrations of the whisker nodes are seen as ellipses, with each dot in the ellipse representing the location of the node in a single video frame (1 ms). Second, as shown in Fig. 3B, the bending magnitude, as well as the amplitude of vibration, increases along the arc length of the whisker from proximal to distal. The increased vibration amplitude is seen as increasing area of the ellipses along the whisker length. Third, Fig. 3B shows that the primary bending direction is in the direction of airflow. The small red arrows indicating bending direction are almost completely parallel with the large blue dashed arrows, indicating the airflow direction.

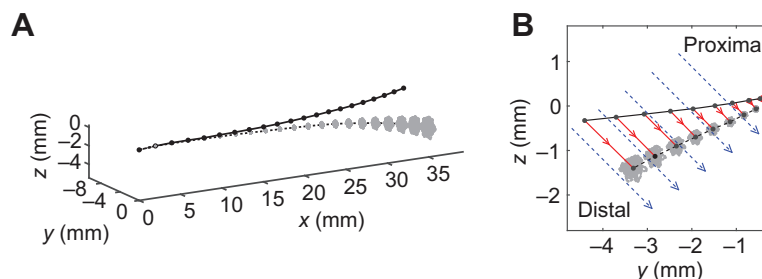


Fig. 3. A whisker will mostly bend in the direction of airflow, and will exhibit vibration about its new mean position. The figures depict the response of the E2 whisker to airflow with speed of 2.3 m s^{-1} . (A) The whisker is oriented 45 deg relative to the airflow and its shape is tracked in both the absence and presence of airflow. The position of the whisker without airflow is shown as a solid black line, with 21 black dots indicating the 21 tracked nodes, spaced 2 mm apart. In the presence of airflow, the whisker deflects to a new mean position (black dashed line) and oscillates about that mean position (ellipses of gray dots). Each dot in each ellipse represents the position of that node in one video frame (1 ms). (B) Projection of the whisker shown in A into the y - z plane. The red solid vectors from the whisker at rest to the whisker's mean position indicate the bending direction of the tracked nodes of the whisker. The magnitude of these vectors increases along the whisker's arc length, as does the amplitude of vibration, as indicated by the increasing size of the gray ellipses. The dashed blue arrows indicate the airflow direction, and are mostly parallel with the vectors indicating the bending direction of the whisker.

Note that the bending direction as defined in Fig. 3 is the direction in which the whisker travels from its resting position to its new mean position. This direction is not always the same as the direction in which the whisker vibrates. In fact, sometimes the vibrations did not even form a well-defined ellipse. The details of vibration magnitude and direction are complex, and will not be further described here.

Bending direction is independent of airflow speed and orientation of the whisker relative to the airflow

Fig. 3 showed only one example in which the primary direction of whisker bending was in the direction of airflow. We carefully examined the effect of speed and orientation angle for all five whiskers. Whisker deflections were recorded at six different airflow speeds, and at five different orientation angles of the whisker relative to the airflow as defined in Fig. 1C (0, 45, 90, 135 and 180 deg).

Fig. 4 confirms that the whisker primarily bends in the direction of airflow, and also shows that the bending direction is independent of airflow speed and whisker orientation relative to the airflow. To create Fig. 4, bending direction was quantified at all tracked nodes of the whisker and averaged to obtain means and standard deviations. Although all plots of Fig. 4 show substantial variability, the average bending direction is always in the direction of flow (0 deg).

Notably, the bending magnitude out of the plane of the airflow direction never exceeded 2.5 deg for any whisker, and its average was 0.0 deg, indicating that out-of-plane motion was equally likely to occur above and below the plane. In contrast, in-plane bending magnitude had a maximum amplitude of 32.5 deg and an average amplitude of 4.4 deg across all nodes and all whiskers.

Bending magnitude increases along the whisker and depends on airflow speed, orientation and whisker geometry

Bending magnitude along the whisker length will be influenced by Reynolds number, material properties of the whisker (density and Young's modulus) and geometric parameters of the whisker (base diameter, arc length, taper and intrinsic curvature). Understanding the effects of all these parameters is challenging. To start, analysis was limited to three major parameters that will strongly influence

bending magnitude: airflow speed, orientation angle and the ratio of whisker length to base diameter (S/D ratio).

Unsurprisingly, bending magnitude was strongly correlated with airflow speed, and was larger at more distal locations along the whisker. This effect is illustrated for two nodes of the α whisker in Fig. 5A. Bending magnitude increases monotonically with airflow speed for both nodes, but is much larger at a node 80% out along the total whisker length than at a node 40% out. These results indicate that the whisker does not bend as a rigid body (see Fig. 2). Although the results of Fig. 5A are shown only for an orientation angle of 0 deg, similar results were found for all orientation angles.

The results shown in Fig. 5A were found to generalize across all whiskers, as shown in Fig. 5B. All whiskers show an approximately linear increase in bending magnitude with airflow speed. Again, results are shown only for an orientation angle of 0 deg, but similar results were found for all orientation angles.

The effect of orientation angle is subtler. At the lowest two airflow speeds (0.5 and 1.4 m s^{-1}), no effect of orientation angle could be observed, and these speeds were excluded from subsequent analysis of orientation angle. At higher airflow speeds (2.2 m s^{-1} and above), systematic variations of bending magnitude with orientation angle were found.

Specifically, for all whiskers, the bending magnitude at orientation angle 0 deg (concave forward into the airflow) was always larger than at any other orientation angle. Fig. 5C shows the bending magnitude at each orientation angle, normalized by the bending magnitude at orientation 0 deg. For the larger three whiskers (E2, α and A2), the curves show a profile that decreases smoothly from 0 to 180 deg. In contrast, the two shorter whiskers (C2 and D5) show a W-shaped profile, with a crest near 90 deg (concave downwards orientation).

Notice that the effects of orientation angle cannot be directly related to whisker length. The fundamental basis for orientation effects must be the whisker's intrinsic curvature, because this is the only parameter that affects the whisker's 3D symmetry. Shorter whiskers have higher intrinsic curvature (Knutsen et al., 2008; Towal et al., 2011; Quist and Hartmann, 2012), explaining why the effect of orientation angle appears to be related to whisker length. From a mechanical point of view, the intrinsic curvature of the whisker allows it to 'twist' about its own axis, and will have a non-linear effect on both axial force and bending (Huet et al., 2015; Huet and Hartmann, 2016). The results for the longer and shorter whiskers are averaged in Fig. 5D, where the smooth drop-off and W shape became even clearer.

Finally, Fig. 5E illustrates how bending magnitude is affected by the S/D ratio for three different airflow speeds. In general, there is an approximately linear trend, such that bending magnitude increases with S/D ratio for all airflow speeds tested. Given that the area moment of inertia (which determines bending) scales as radius to the fourth power, it makes good intuitive sense that a whisker with a low S/D ratio will bend less than a whisker with a large S/D ratio.

The whisker vibrates at frequencies correlated with its resonance modes

Like all mechanical systems, whiskers tend to vibrate near their resonance frequencies (Hartmann et al., 2003; Neimark et al., 2003; Andermann et al., 2004; Ritt et al., 2008; Boubenec et al., 2012; Yan et al., 2013). Making the standard assumption that a whisker is linearly tapered (Ibrahim and Wright, 1975; Williams and Kramer, 2010; Quist et al., 2011; Hires et al., 2013) and can be modeled as a

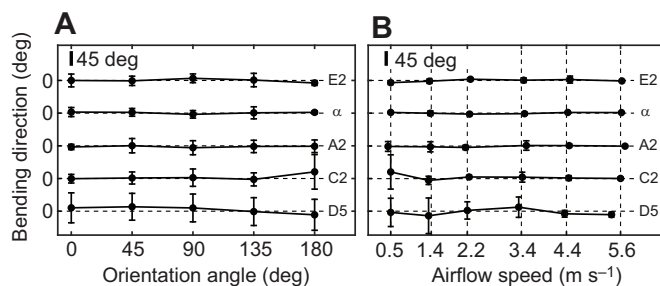


Fig. 4. Bending direction does not vary systematically with orientation angle or airflow speed. In both plots whiskers are ordered by length, from longest (E2) to shortest (D5). The bending direction was averaged over all nodes except the first node at the base of the whisker, because it is fixed. (A) Mean and standard deviation of bending direction as a function of orientation angle for all five whiskers. Data are averaged over all six airflow speeds. (B) Mean and standard deviation of bending direction as a function of airflow speed for all five whiskers. Data are averaged over all five orientation angles. Notice that there is small variability in airflow speed for different whiskers, which is observed as small shifts in the placement of the data points on the x-axis. In both A and B, variability in bending direction is larger for shorter whiskers than for longer whiskers because measurement error was greater for smaller deflections.

fixed-free conical beam (Georgian, 1965), the whisker’s resonant frequency can be computed according to Eqn 2.

We aimed to compare whisker vibrations with their theoretical resonance profiles; however, under the influence of airflow, whiskers were observed to vibrate in all three dimensions, and in many cases the major axis of vibration was challenging to define. In performing the vibration analysis we had to make two choices: first, which direction of motion to analyze; and second, which node out along the whisker arc length to analyze.

To decide on the direction of motion to analyze, we first quantified vibration magnitude and frequency in the *x*-, *y*- and *z*-directions, as defined in Fig. 1A. The *y*- and *z*-directions are both transverse to the base of the whisker, whereas the *x*-direction is directed axially. Unsurprisingly, vibrations in the *y*- and *z*-directions were similar in both magnitude and frequency, whereas vibrations in the *x*-direction were much smaller and more variable in magnitude. Because results in *y*- and *z*-directions were so similar, results show only the frequency content of the vibration in the *y*-direction.

To decide on which node to analyze, we examined the frequency content at each node individually. At proximal nodes, the vibration magnitude was so small that the frequency was challenging to identify, whereas at distal nodes the vibration magnitude was large, but only the first mode of vibration could be observed. We ultimately chose to perform the frequency analysis at a node 40% out along the whisker arc length because the vibration magnitude was large enough to permit accurate measurement and multiple modes of vibration could be observed.

With these choices made, Fig. 6A shows the frequency content of vibrations of all five whiskers in response to airflow at a speed close to 5.6 m s⁻¹. Results for all five whiskers are averaged over the five orientation angles. Because the resonance peaks are broad, however, it is challenging to estimate the peak frequencies. For example, the first mode of whisker A2 does not have a well-defined peak.

To address this problem, we found the ‘widest possible range’ for each resonance mode using Eqn 2. In Fig. 6A, the widest possible ranges for the first, second and third resonance modes are

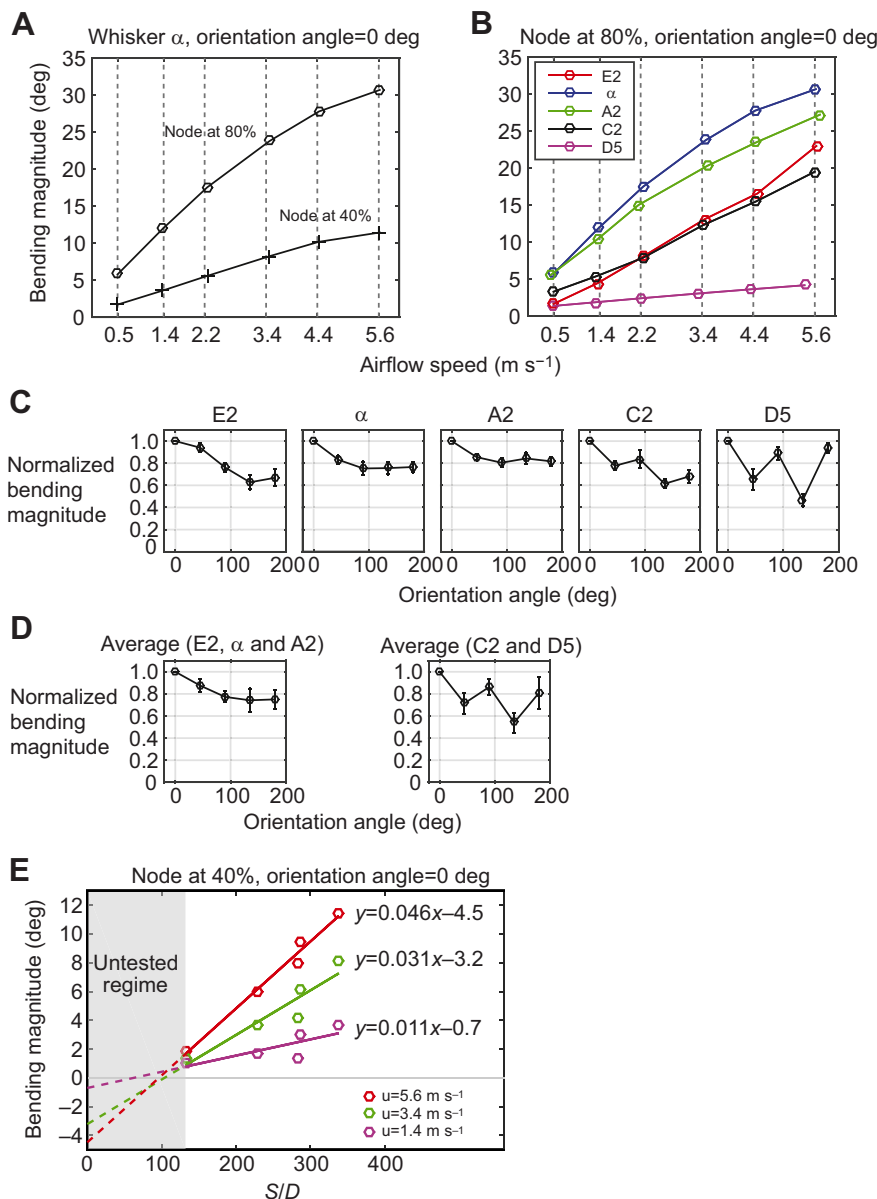


Fig. 5. Bending magnitude depends on airflow speed, orientation angle of the whisker, and the whisker’s arc-length to base diameter (*S/D*) ratio.

(A) The bending magnitude of whisker α at an orientation of 0 deg relative to the airflow is shown for nodes 40% and 80% out along the whisker length. (B) Bending magnitude of all five whiskers increases monotonically with airflow speed. Results are shown for whiskers oriented 0 deg relative to the airflow and for nodes 80% out along the whisker length. (C) For each whisker, normalized bending magnitude varies with orientation angle. Bending magnitude was normalized by that whisker’s largest bending magnitude, which was always found at an orientation angle of 0 deg (concave forwards, toward the airflow). The normalized bending magnitude at each orientation angle is averaged over the four highest airflow speeds. Data are shown for a node 40% out along the whisker length. (D) For the three larger whiskers (E2, α and A2), normalized bending magnitude decreases smoothly with orientation angle, while for the two shorter whiskers (C2 and D5) the relationship is W shaped. These results are averages of those shown in C. (E) Bending magnitude increases approximately linearly with the arc length to diameter (*S/D*) ratio of the whisker. The whisker identities are D5, C2, E2, A2 and α , ordered from small to large *S/D* ratios. Note that the *S/D* ratio for E2 is only slightly smaller than that for A2. Results are shown for a node 40% out along each whisker and at airflow speeds (*u*) of 1.4, 3.4 and 5.6 m s⁻¹. Linear fits between bending magnitude and the *S/D* ratio show increasing slopes with airflow speed. Because the airflow speeds were not identical for all five whiskers, values of bending magnitude have been interpolated between the airflow speeds closest to the speed of interest.

highlighted in yellow, cyan and green, respectively. The points at which the mean amplitude spectrum intersected the boundaries of these ranges were connected by imaginary line segments, and the vertical distance from the segments to the mean amplitude spectrum was found at each frequency. The largest distance was taken to define the crest of the spectrum, and the corresponding frequency was considered to be the resonance frequency for that mode. This procedure allowed us to establish a single experimentally measured value for each resonance mode.

To compare observed and predicted resonance frequencies, Young's modulus was left as a free parameter and optimized by minimizing the summed squared error between predicted and experimental values, for all frequency modes, for all five whiskers.

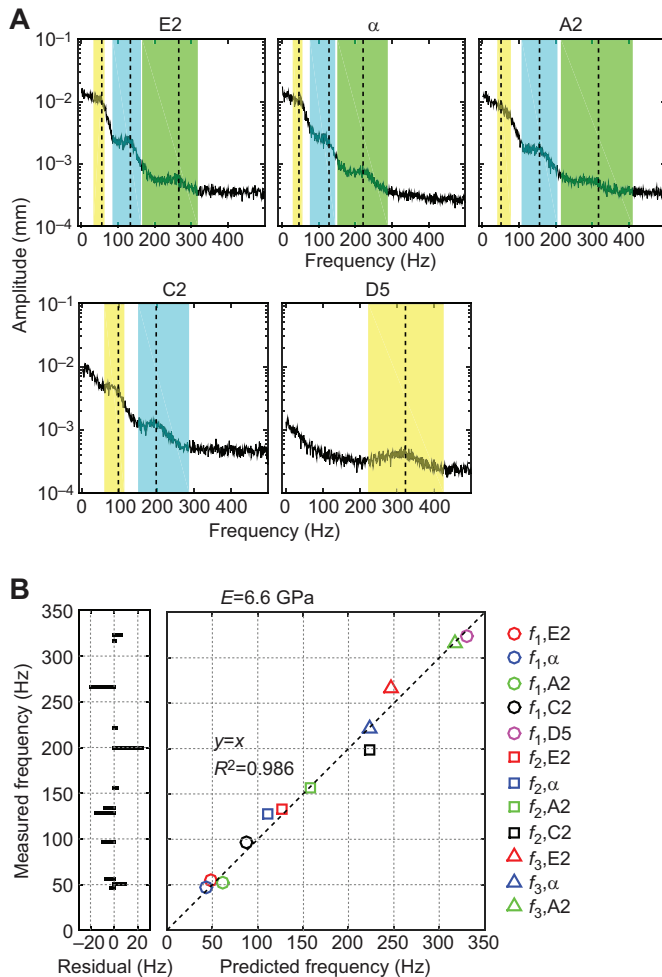


Fig. 6. The vibration frequencies of a whisker are correlated with its resonance modes. (A) The average y -amplitude as a function of frequency in units of mm (mean amplitude spectrum) is shown for all five whiskers for an airflow speed close to 5.6 m s^{-1} . Vibrations were measured in the y -direction, that is, transverse to the whisker and parallel to the ground. All position data were obtained from the tracked node closest to 40% out along the total whisker length. Data have been averaged across all orientation angles relative to the airflow. Whiskers E2, α and A2 show three clear resonance modes, C2 shows two resonance modes, and D5 shows only the first mode resonance. The regions highlighted in yellow, cyan and green indicate the widest possible range for each resonance mode, found by inserting Young's modulus (E)=3 or 11 GPa into Eqn 2. The vertical dashed lines indicate the peak of the amplitude spectrum within that resonance range. (B) Comparison of experimental and theoretical values for the resonance frequencies shows an excellent match. The best linear fit between predicted and measured values for all modes of all five whiskers was found with Young's modulus set to 6.6 GPa.

A best fit between predicted and observed resonance frequencies was obtained with a Young's modulus of 6.6 GPa ($R^2=0.986$; Fig. 6B).

Computing mechanical responses to airflow across the entire vibrissal array

The previous sections have indicated that a vibrissa's response to airflow depends not only on airflow speed, but also on the whisker's orientation relative to the airflow and on the S/D ratio. As shown in Fig. 7A, the rat's vibrissae are arranged in a regular array of rows and columns on the cheek. Their orientation and geometry varies systematically across the array (Ibrahim and Wright, 1975; Brecht et al., 1997; Diamond et al., 2008; Towal et al., 2011). We used these systematic variations to estimate how the vibrissal response to airflow will vary across the array.

We began by accounting for the whisker's geometric parameters: the orientation of its intrinsic curvature on the rat's face, and the whisker's arc length, base diameter and S/D ratio.

Orientation of the whisker's intrinsic curvature. Previous work has shown that each whisker has a unique intrinsic curvature (Knutsen et al., 2008; Towal et al., 2011). The orientation of the intrinsic curvature shifts smoothly from concave downwards in caudal regions of the array to concave forward in more rostral regions. This smooth variation is depicted in Fig. 7B; the equation for orientation as a function of the (row, column) position of the whisker is $\zeta=18.8col-11.4row-5.0$ (Towal et al., 2011).

Arc length (S). Whisker arc length increases with column (from rostral to caudal), with a weak dependence on row, as shown in Fig. 7C. The equation for arc length as a function of (row, column) position is $S=-7.9col+2.2row+52.1$ (Towal et al., 2011).

Base diameter (D). To date, whisker diameter has not been characterized as a function of (row, column) position; however, previous work found a power law relationship between base diameter and whisker arc length (Hartmann et al., 2003; Neimark et al., 2003). We confirmed this relationship using data obtained from 244 whiskers in a concurrent study. Results are shown in Fig. 7D. The best-fit equation was found to be: $D=24.1S^{0.53}$. Note that D has units of μm , whereas S has units of mm.

S/D ratio. Finally, we used the equations from Fig. 7C,D to compute the S/D ratio for each whisker, as illustrated in Fig. 7E.

The parameters identified in Fig. 7 allow us to combine the orientation and geometric data with the empirical relationships found in Fig. 5 to simulate how bending magnitude will vary across the vibrissal array for three different airflow speeds. These simulations were run as follows. (1) The airflow direction was assumed to be horizontal, parallel with the ground. (2) The simulated rat was assumed to have a level head pitch, parallel to the ground as depicted in Fig. 7A. The head pitch determines each whisker's orientation relative to the (horizontal) airflow. (3) The S/D ratio for each whisker was determined from Fig. 7E. Three whiskers (C6, D6 and E6) were excluded from analysis because their S/D ratios were less than 132, within the untested regime of Fig. 5E. (4) Given the S/D ratio of each whisker and an airflow speed, the equations of Fig. 5E were used to compute the whisker's bending magnitude, for a node 40% from the base and an orientation angle of 0 deg. (5) To account for each whisker's orientation relative to the airflow, results were scaled by the ratios shown in Fig. 5D. Whiskers

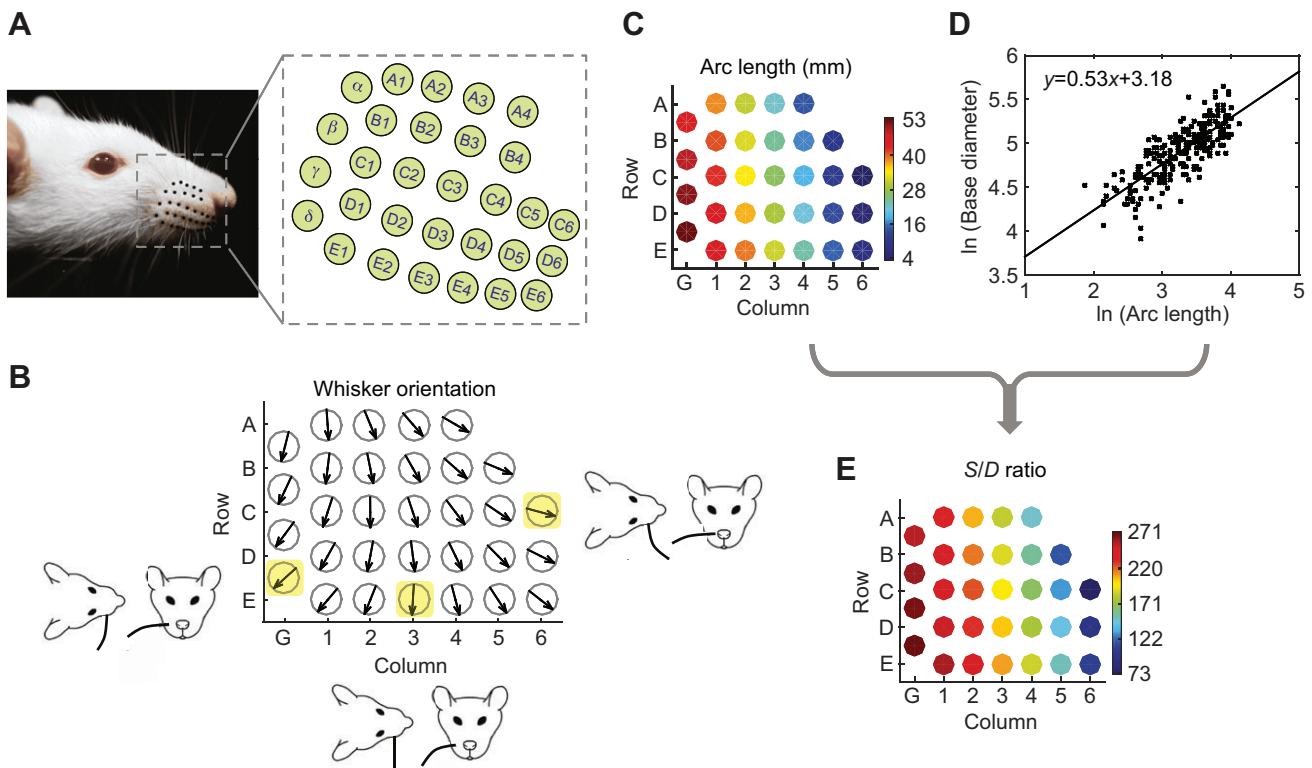


Fig. 7. Parameters used to calculate bending magnitude and vibration frequency in response to airflow. (A) A photo of a rat whisker pad with whisker basepoints enhanced as black dots. Whiskers are arranged in an array and named by their (row, column) identity. (B) Whisker orientation across the array when the rat's head is approximately level and the whiskers are at rest. The circles represent the vibrissal base points. The arrow in each circle is a direction vector that indicates the concave-forward direction of the vibrissa's intrinsic curvature. Three examples (highlighted in yellow) are shown to improve intuition for how the orientation of whisker curvature varies across the array. (C) Arc length varies strongly with column and weakly with row across the whisker array (data from Towal et al., 2011). (D) An analysis of 244 whiskers showed that a power law adequately described the relationship between base diameter (μm) and arc length (mm). (E) The S/D ratio increases from rostral to caudal with a smaller dependence on row.

with S/D ratios greater than 250 were assumed to follow the smooth, 'large whisker' average, whereas whiskers with S/D ratios smaller than 250 were assumed to follow the W-shaped 'small whisker' average.

Simulation results are shown in Fig. 8. At a single airflow speed (Fig. 8A), the dominant effect is the S/D ratio. Bending magnitude decreases from the Greek column (G) to column 5. Smaller variations are seen from row E to row A. The trend with column

remains close to linear across the full range of airflow speeds (Fig. 8B).

A similar analysis was performed for vibration frequency (Fig. 8C,D). This required an estimate of each whisker's tip diameter, but the tips of the 244 whiskers shown in Fig. 7D were often significantly damaged. Fortunately, tip diameter has only a small effect on frequency (Georgian, 1965), so the average value, $6\ \mu\text{m}$, was used for all whiskers.

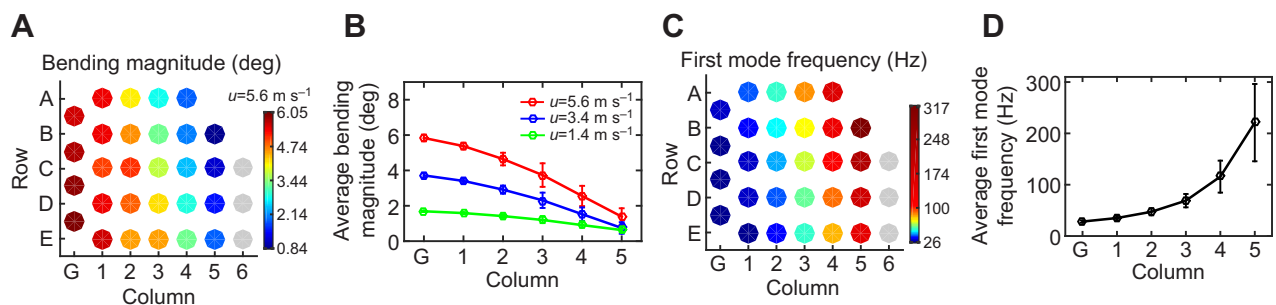


Fig. 8. Bending magnitude and vibration frequency in response to airflow predicted across the full array of whiskers. (A) Predicted bending magnitude at nodes 40% out along each whisker in response to airflow with a speed $u = 5.6\ \text{m s}^{-1}$. Overall, bending closely follows the S/D ratio shown in Fig. 7E. The three most rostral whiskers are omitted from this analysis because they fall into the 'untested regime' of Fig. 5E. (B) Bending magnitude as a function of column (averaged across rows) is predicted for three different airflow speeds. (C) Predicted first mode resonance frequencies across the whisker array. Vibration frequency increases from caudal to rostral. Note that the color bar is very non-linear. (D) The predicted first mode frequency is shown as a function of column, averaged across rows.

Inserting the values of base diameter, tip diameter, arc length, the best-fit value for Young's modulus (6.6 GPa) and the average density (1300 kg m⁻³) into the equation for whisker resonance (Eqn 2), we predicted the first mode resonance frequency of all whiskers. As shown in Fig. 8C,D, the first mode resonance frequency increases from column G to column 5 as the whiskers become shorter.

Thus bending and vibrations are complementary: larger, more caudal whiskers will experience larger bending magnitudes but lower frequency vibrations, whereas shorter, more rostral whiskers will experience smaller bending magnitudes but higher frequency vibrations.

The effect of head pitch and whisking motions on the response of vibrissae across the array

During 'whisking' behavior, rats rhythmically sweep the macrovibrissae between 5 and 25 Hz (Welker, 1964; Carvell and Simons, 1990). Rats also often pitch their heads up and down during navigation and tactile exploration. Both head and whisker motions will significantly change the whisker orientation relative

to the airflow, which will affect bending magnitude (Fig. 5C). We used the same approach as in Fig. 8 to investigate the effect of head pitch and whisking on the response of vibrissae across the array.

The simulated bending magnitudes of the vibrissae at rest at two different head pitches are shown in Fig. 9A. Pitching the head upwards tends to increase bending magnitude because most whiskers will tend to orient more concave forwards towards the airflow (see Fig. 5D).

We then simulated a 60 deg whisker protraction using kinematic equations obtained from behaving rats, which include the effects of dorsal-ventral elevation as well as the whisker's roll about its own axis (Knutzen et al., 2008). Simulated bending magnitudes for the array of protracted whiskers are shown in Fig. 9B, again for two head pitches. As in Fig. 9A, increasing head pitch increases overall bending magnitude.

Comparing Fig. 9A and B, we see that whisker protraction causes more whiskers to orient concave forward into the airflow, producing an increase in the range of bending magnitudes for a given column.

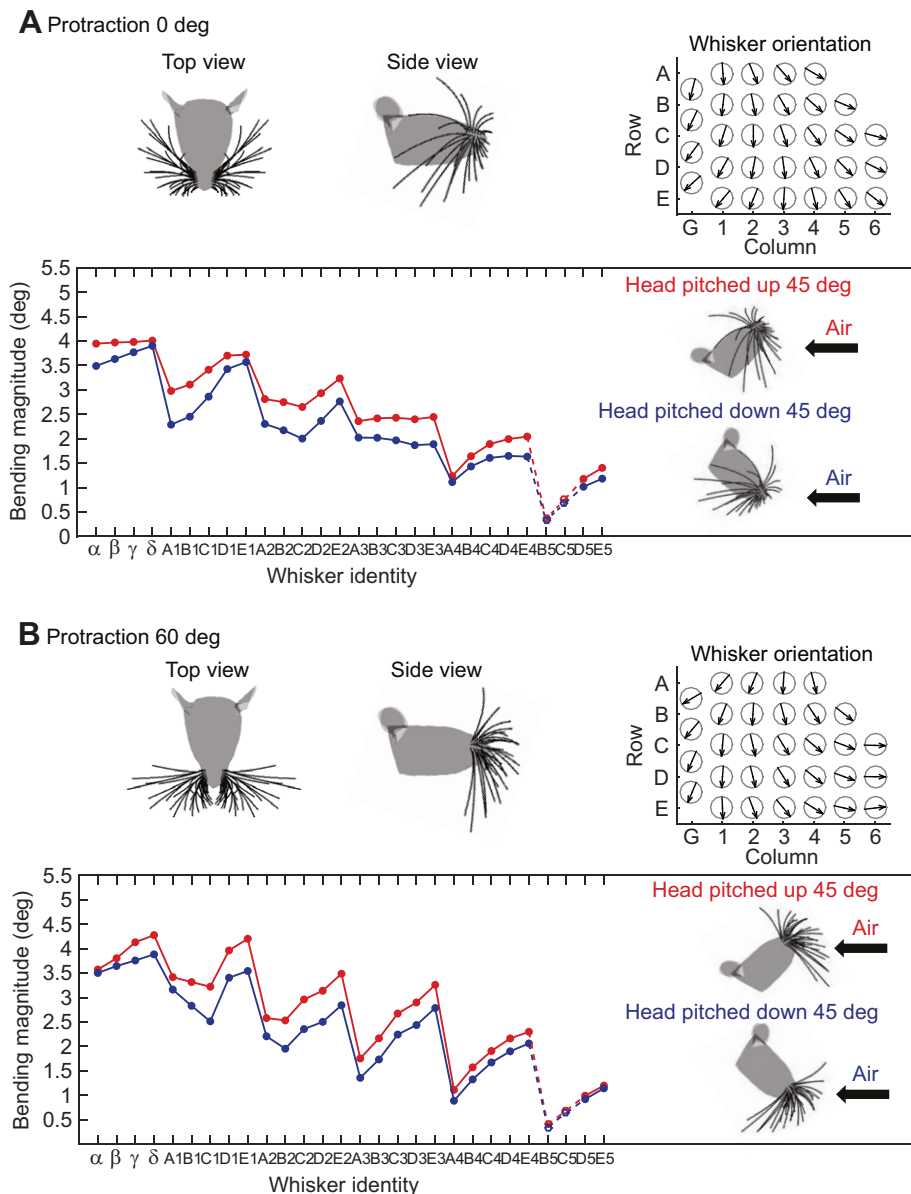


Fig. 9. The effect of head pitch and whisking motions on the bending magnitude of vibrissae across the array. In both A and B, the images of the rat head provide visual intuition for the configuration of the whisker array at rest in top and side views. The top right graph in both subplots shows the orientation of the intrinsic curvature of each vibrissa, using the same convention as in Fig. 7B. The arrow in each circle is a direction vector that indicates the concave-forward direction of the vibrissa's intrinsic curvature. The x-axis in both subplots is linear with column, consistent with the approximately linear caudorostral spacing of the whiskers on the mystacial pad (Towal et al., 2011; Brecht et al., 1997). (A) Predicted bending magnitude at nodes 40% out along each whisker in response to airflow at 3.4 m s⁻¹. The vibrissae are simulated to be at rest with the rat's head pitched either up or down by 45 deg. (B) Predicted bending magnitude at nodes 40% out along each whisker in response to airflow at 3.4 m s⁻¹. The vibrissae are simulated to have protracted by 60 deg, with the rat's head pitched either up or down by 45 deg.

It is crucial to note, however, that these simulations do not include the effects of changes in rostrocaudal angles; the simulations reveal only the effects of the changing orientation angles during protraction.

The results shown in Figs 5, 8 and 9 are subject to two important caveats: experiments were performed on isolated whiskers, and airflow was always directed perpendicular to the whisker length. In reality, the rat's head will affect the flow field around each whisker, and whiskers will emerge from the face at many different angles relative to the flow. Although more experiments are required to investigate these effects, the general trends revealed by Figs 5, 8, and 9 support the conclusion that the rat has a rich motor repertoire for flow exploration.

DISCUSSION

The vibrissae are multimodal sensors, responsive to both touch and airflow

Although it is common wisdom that terrestrial mammals can sense and follow the wind, the cues that underlie this ability are virtually unstudied. To our knowledge, the only study of anemotaxis in terrestrial mammals investigated the behavior of marsh rice rats (*Oryzomys palustris*) (Schooley and Branch, 2005). Rats were released outdoors at a fixed location but at a random orientation. They moved either upwind or downwind 82% of the time, and rarely moved crosswind. Multiple cues could subservise this behavior, including motion of the fur, thermal signals from glabrous skin, and, as suggested by the present study, mechanical signals from the macrovibrissae.

The present work demonstrates that macrovibrissae respond to airflows as small as 0.5 m s^{-1} (Fig. 5), certainly sensitive enough to respond to typical air currents on land (Monahan et al., 2011). Furthermore, because most whiskers are oriented concave forward or concave down, the mechanical response to airflow will be amplified compared with a concave backwards orientation.

The macrovibrissae transmit multiple cues about flow velocity: the whisker bends in the flow direction and oscillates around its new static position (Fig. 3). The bending magnitude varies systematically with airflow speed, whisker geometry, and the whisker's orientation relative to the airflow (Fig. 5), but bending direction is largely unaffected by these parameters (Fig. 4). Vibration magnitude was not addressed here but is an important future topic for investigation.

Taken together, these results suggest that, as is the case for marine mammals (Dehnhardt and Ducker, 1996; Gläser et al., 2011; Grant et al., 2013b), the vibrissae of rodents can sense both flow and touch.

The mechanics of airflow versus touch

Although vibrissae will respond to mechanical stimulation generated by either touch or airflow, their response to these two types of stimuli will differ in several important ways.

First, a directional airflow stimulus will cause all whiskers to bend in the same general direction. In contrast, when the whiskers are protracted against an object, they will tend to slip in different directions depending on their kinematic trajectory, their intrinsic curvature, object geometry and friction (Solomon and Hartmann, 2008, 2010; Hobbs et al., 2016; Huet et al., 2015; Huet and Hartmann, 2016).

Second, the vibrations generated by airflow will be different than those generated by tactile collision. Airflow will tend to cause all whiskers to vibrate simultaneously near their resonance frequencies (Fig. 6). The vibrations will be superposed on bending, and will be sustained as long as airflow continues. In contrast, during tactile

contact, vibration frequencies will depend in complex ways on intrinsic whisker dynamics, the location (along the whisker length) of whisker–object contact, object surface texture, stick-slip and friction (Ritt et al., 2008; Wolfe et al., 2008). In addition, vibrations will damp as the whisker increasingly presses against the object (Boubenec et al., 2012; Quist et al., 2014; Hobbs et al., 2016). If all whiskers simultaneously deflect past an edge, they will vibrate near resonance, but vibrations will damp and will not be superposed on a quasistatic bend.

Third, airflow will generate a unique relationship between bending and vibrations across the whiskers of the array. Fig. 8 of the present study finds an inverse relationship between bending magnitude and vibration frequency. Longer whiskers will bend more in response to airflow, but vibrate at lower frequencies than shorter whiskers. Tactile stimuli will not generate such a systematic relationship across the array.

Finally, the touch of a whisker against an object generally creates forces restricted to a small region along the vibrissal length. Many instances of vibrissal touch can be approximated as point load deflections. In contrast, airflow exerts a distributed load along the whisker length. Although for any distributed load there is an equivalent point load that generates the same total force and moment at the whisker base, the whisker's shape will be different between the two loading conditions. The whisker's shape will in turn affect its response to continued loading, so the vibrations that ensue from whisker touch will be different than those generated by airflow.

Comparison with tactile and flow-sensing hairs of arthropods

Unlike vibrissae, which respond to both touch and airflow, arthropods hairs are functionally segregated (Dechant et al., 2006). Tactile hairs are between 1 and 3 mm long and bend in response to deflection, whereas flow-sensing hairs are shorter ($<1 \text{ mm}$) and rotate, but do not bend, in response to airflow (Albert et al., 2001; Magal et al., 2006; Humphrey and Barth, 2007).

We suggest that two geometric features of vibrissae grant them the multimodal capacity evolutionarily denied to arthropod hairs: (1) vibrissae are much longer than arthropod hairs; and (2) each vibrissa is held tightly at its base (Bagdasarjan et al., 2013), whereas arthropod flow-sensing hairs are held loosely by a socket (Barth, 2004).

Because the vibrissae are long, their mechanical response is unaffected by the boundary layer around the animal's face, and their spacing precludes viscous coupling. In addition, because they are held stiffly at their base, they primarily bend (instead of rotate) in response to airflow, and the bending magnitude depends on airflow speed.

In contrast, most flow-sensing hairs on arthropods are so short that they lie within the boundary layer, whose thickness depends on flow oscillation frequency. Thus the hairs will respond maximally to oscillating flow that generates a boundary layer thickness equal to the hair length, instead of responding directly to flow velocity (Humphrey and Barth, 2007). In addition, the mechanical response of some (though not all) arthropod hairs is subject to viscous coupling (Humphrey et al., 1993; Magal et al., 2006; Dangles et al., 2007; Humphrey and Barth, 2007; Bathellier et al., 2012), further complicating the relationship between maximal response and flow speed. Finally, arthropod hairs longer than 1 mm do not vibrate at their resonance frequencies because of the weak restoring force of the socket (Humphrey and Barth, 2007; Casas et al., 2010).

These comparisons highlight the wide variety of functions for flow sensors. In both air and water, flow sensors are used in rapid detection behaviors (Barth et al., 1995; Barth, 2002; Shimozawa et al., 2003),

oriented escape (Jacobs, 1995; Catania, 2009), directional navigation (Casas and Dangles, 2010; Reep et al., 2011), odor following (Reidenbach and Koehl, 2011) and complex perceptual investigation of flow profiles (Dehnhardt et al., 2001). The geometry of a flow sensor is expected to match its function and to exploit a trade-off between response reliability and spatial specificity. For example, if hairs are viscously coupled, a larger number of hairs will respond to a flow stimulus but at the expense of single-hair precision.

The geometry of arthropod flow-sensing hairs is well suited to facilitate rapid detection and escape. The geometry of a vibrissa will superpose vibration on bending, and the relationship between these signals may provide cues about flow distinct from the sense of touch. We therefore suggest that whiskers may specifically be involved in sensing complex flow profiles for anemotaxis, similar to vibrissal-based hydrodynamic trail-following in pinnipeds (Dehnhardt et al., 2001; Gläser et al., 2011; Miersch et al., 2011; Wieskotten et al., 2011). Although fluid vortices dissipate rapidly in air, differential responses across the vibrissal array could allow a rat to sense a wake around a distant obstruction or the spatiotemporal structure of flow carrying an odor.

Whisker protraction and head pitch permit active exploration of the flow profile

If, as we suggest, the vibrissae play a role in sensing complex flow profiles, then we expect the rat to have the ability to actively probe flow structure by adjusting its sensors. Accordingly, Figs 8 and 9 indicate that the rat can change the orientation of its whiskers either via head movements or by whisking. Changing the orientation angles of the whiskers will alter bending magnitudes in complex ways that depend strongly on intrinsic whisker curvature (Fig. 5B), which varies systematically across the array. Active exploration of flow structure may help the rat distinguish between externally generated flow and flow generated by locomotion, typically near $\sim 1 \text{ m s}^{-1}$ (Arkley et al., 2014).

When taken with the recent discovery that whisking and sniffing are synchronized by a common central pattern generator (Moore et al., 2013), the present work suggests that vibrissotactile sensation may be important to olfactory search behaviors. Neurons in the trigeminal pathway respond strongly to airpuffs, and the present work demonstrates not only that vibrissae are mechanically sensitive to airflow, but also that the rat could actively adjust how the vibrissae respond to airflow. Given that an animal's nervous system coevolves with its ability to move so as to gather particular types of sensory information, the potential anemotaxic role of vibrissae in odor localization could be key to understanding processing in the vibrissotrigeminal system.

Acknowledgements

We thank Venkatesh Gopal, Yan B. Man and Neelesh A. Patankar for useful discussions, Brian W. Quist for writing code to perform three-dimensional tracking of the whiskers, and Hayley M. Belli for whisker length and diameter measurements.

Competing interests

The authors declare no competing or financial interests.

Author contributions

M.J.Z.H. conceived the project. Y.S.W.Y., M.M.G. and M.J.Z.H. designed the experiments, analyzed data and wrote the paper. Y.S.W.Y. and M.M.G. performed the experiments.

Funding

This work was supported by National Science Foundation awards CRCNS-IIS-1208118, CAREER IOS-0846088 and EFRI-0938007, and National Institutes of Health award R01NS093585 to M.J.Z.H. Deposited in PMC for release after 6 months.

Supplementary information

Supplementary information available online at <http://jeb.biologists.org/lookup/suppl/doi:10.1242/jeb.126896/-/DC1>

References

- Albert, J., Friedrich, O., Dechant, H.-E. and Barth, F. (2001). Arthropod touch reception: spider hair sensilla as rapid touch detectors. *J. Comp. Physiol. A Sens. Neural. Behav. Physiol.* **187**, 303–312.
- Andermann, M. L., Ritt, J., Neimark, M. A. and Moore, C. I. (2004). Neural correlates of vibrissa resonance: band-pass and somatotopic representation of high-frequency stimuli. *Neuron* **42**, 451–463.
- Arkley, K., Grant, R. A., Mitchinson, B. and Prescott, T. J. (2014). Strategy change in vibrissal active sensing during rat locomotion. *Curr. Biol.* **24**, 1507–1512.
- Bagdasarian, K., Szwed, M., Knutsen, P. M., Deutsch, D., Derdikman, D., Pietr, M., Simony, E. and Ahissar, E. (2013). Pre-neuronal morphological processing of object location by individual whiskers. *Nat. Neurosci.* **16**, 622–631.
- Barth, F. G. (2002). Spider senses – technical perfection and biology. *Zoology* **105**, 271–285.
- Barth, F. G. (2004). Spider mechanoreceptors. *Curr. Opin. Neurobiol.* **14**, 415–422.
- Barth, F. G., Humphrey, J. A. C., Wastl, U., Halbritter, J. and Brittinger, W. (1995). Dynamics of arthropod filiform hairs. III. Flow patterns related to air movement detection in a spider (*Cupiennius salei* Keys). *Philos. Trans. R. Soc. B Biol. Sci.* **347**, 397–412.
- Bathellier, B., Steinmann, T., Barth, F. G. and Casas, J. (2012). Air motion sensing hairs of arthropods detect high frequencies at near-maximal mechanical efficiency. *J. R. Soc. Interface* **9**, 1131–1143.
- Bosman, L. W. J., Houweling, A. R., Owens, C. B., Tanke, N., Shevchouk, O. T., Rahmati, N., Teunissen, W. H. T., Ju, C., Gong, W., Koekoek, S. K. E. et al. (2011). Anatomical pathways involved in generating and sensing rhythmic whisker movements. *Front. Integr. Neurosci.* **5**, 53.
- Boubenec, Y., Shulz, D. E. and Debrégeas, G. (2012). Whisker encoding of mechanical events during active tactile exploration. *Front. Behav. Neurosci.* **6**, 73.
- Bouguet, J. (2013). Camera calibration toolbox for Matlab. Available at http://www.Vision.Caltech.Edu/bouguetj/calib_doc/.
- Brecht, M., Preilowski, B. and Merzenich, M. M. (1997). Functional architecture of the mystacial vibrissae. *Behav. Brain Res.* **84**, 81–97.
- Carvell, G. E. and Simons, D. J. (1990). Biometric analyses of vibrissal tactile discrimination in the rat. *J. Neurosci.* **10**, 2638–2648.
- Casas, J. and Dangles, O. (2010). Physical ecology of fluid flow sensing in arthropods. *Annu. Rev. Entomol.* **55**, 505–520.
- Casas, J., Steinmann, T. and Krijnen, G. (2010). Why do insects have such a high density of flow-sensing hairs? Insights from the hydromechanics of biomimetic MEMS sensors. *J. R. Soc. Interface* **7**, 1487–1495.
- Catania, K. C. (2009). Tentacled snakes turn c-starts to their advantage and predict future prey behavior. *Proc. Natl. Acad. Sci. USA* **106**, 11183–11187.
- Dangles, O., Pierre, D., Christides, J. P. and Casas, J. (2007). Escape performance decreases during ontogeny in wild crickets. *J. Exp. Biol.* **210**, 3165–3170.
- Dechant, H.-E., Hößl, B., Rammerstorfer, F. G. and Barth, F. G. (2006). Arthropod mechanoreceptive hairs: modeling the directionality of the joint. *J. Comp. Physiol. A* **192**, 1271–1278.
- Dehnhardt, G. and Ducker, G. (1996). Tactual discrimination of size and shape by a California sea lion (*Zalophus californianus*). *Anim. Learn. Behav.* **24**, 366–374.
- Dehnhardt, G., Mauck, B., Hanke, W. and Bleckmann, H. (2001). Hydrodynamic trail-following in harbor seals (*Phoca vitulina*). *Science* **293**, 102–104.
- Diamond, M. E., von Heimendahl, M., Knutsen, P. M., Kleinfeld, D. and Ahissar, E. (2008). 'Where' and 'what' in the whisker sensorimotor system. *Nat. Rev. Neurosci.* **9**, 601–612.
- Georgian, J. C. (1965). Discussion: 'Vibration frequencies of tapered bars and circular plates' (Conway, H. D., Becker, E. C. H., and Dubil, J. F., 1964, *ASME J. Appl. Mech.*, 31, pp. 329–331). *J. Appl. Mech.* **32**, 234–235.
- Gläser, N., Wieskotten, S., Otter, C., Dehnhardt, G. and Hanke, W. (2011). Hydrodynamic trail following in a California sea lion (*Zalophus californianus*). *J. Comp. Physiol. A* **197**, 141–151.
- Grant, R. A., Haidarliu, S., Kennerley, N. J. and Prescott, T. J. (2013a). The evolution of active vibrissal sensing in mammals: evidence from vibrissal musculature and function in the marsupial opossum *Monodelphis domestica*. *J. Exp. Biol.* **216**, 3483–3494.
- Grant, R., Wieskotten, S., Wengst, N., Prescott, T. and Dehnhardt, G. (2013b). Vibrissal touch sensing in the harbor seal (*Phoca vitulina*): how do seals judge size? *J. Comp. Physiol. A* **199**, 521–533.
- Grasso, F. W. and Basil, J. A. (2002). How lobsters, crayfishes, and crabs locate sources of odor: current perspectives and future directions. *Curr. Opin. Neurobiol.* **12**, 721–727.
- Hanke, W., Wieskotten, S., Marshall, C. and Dehnhardt, G. (2013). Hydrodynamic perception in true seals (Phocidae) and eared seals (Otiariidae). *J. Comp. Physiol. A* **199**, 421–440.

- Hartmann, M. J.** (2001). Active sensing capabilities of the rat whisker system. *Auton. Rob.* **11**, 249–254.
- Hartmann, M. J., Johnson, N. J., Towal, R. B. and Assad, C.** (2003). Mechanical characteristics of rat vibrissae: resonant frequencies and damping in isolated whiskers and in the awake behaving animal. *J. Neurosci.* **23**, 6510–6519.
- Hires, S. A., Pammer, L., Svoboda, K. and Golomb, D.** (2013). Tapered whiskers are required for active tactile sensation. *Elife* **2**, e01350.
- Hobbs, J. A., Towal, R. B. and Hartmann, M. J. Z.** (2016). Spatiotemporal patterns of contact across the rat vibrissal array during exploratory behavior. *Front. Behav. Neurosci.* **9**, doi:10.3389/fnbeh.2015.00356.
- Huet, L. A. and Hartmann, M. J. Z.** (2016). Simulations of a vibrissa slipping along a straight edge and an analysis of frictional effects during whisking. *IEEE Trans. Haptics*. (in press) doi:10.1109/TOH.2016.2522432.
- Huet, L. A., Schroeder, C. L. and Hartmann, M. J. Z.** (2015). Tactile signals transmitted by the vibrissa during active whisking behavior. *J. Neurophys.* **113**, 3511–3518.
- Humphrey, J. A. C. and Barth, F. G.** (2007). Medium flow-sensing hairs: biomechanics and models. In *Advances in Insect Physiology: Insect Mechanics and Control*, Vol. 34 (ed. J. Casas), pp. 1–80. San Diego, CA: Elsevier Academic Press Inc.
- Humphrey, J. A. C., Devarakonda, R., Iglesias, I. and Barth, F. G.** (1993). Dynamics of arthropod filiform hairs. I. Mathematical modelling of the hair and air motions. *Philos. Trans. R. Soc. B Biol. Sci.* **340**, 423–444.
- Ibrahim, L. and Wright, E. A.** (1975). Growth of rats and mice vibrissae under normal and some abnormal conditions. *J. Emb. Exp. Morph.* **33**, 831–844.
- Jacobs, G. A.** (1995). Detection and analysis of air currents by crickets – a special insect sense. *Bioscience* **45**, 776–785.
- Keil, T. A.** (2012). Sensory cilia in arthropods. *Arth. Struct. Dev.* **41**, 515–534.
- Knutsen, P. M., Biess, A. and Ahissar, E.** (2008). Vibrissal kinematics in 3d: tight coupling of azimuth, elevation, and torsion across different whisking modes. *Neuron* **59**, 35–42.
- Kuruppath, P., Gugig, E. and Azouz, R.** (2014). Microvibrissae-based texture discrimination. *J. Neurosci.* **34**, 5115–5120.
- Magal, C., Dangles, O., Caparroy, P. and Casas, J.** (2006). Hair canopy of cricket sensory system tuned to predator signals. *J. Theor. Biol.* **241**, 459–466.
- Miersch, L., Hanke, W., Wieskotten, S., Hanke, F. D., Oeffner, J., Leder, A., Brede, M., Witte, M. and Dehnhardt, G.** (2011). Flow sensing by pinniped whiskers. *Philos. Trans. R. Soc. B Biol. Sci.* **366**, 3077–3084.
- Monahan, A. H., He, Y., McFarlane, N. and Dai, A.** (2011). The probability distribution of land surface wind speeds. *J. Climate* **24**, 3892–3909.
- Moore, J. D., Deschênes, M., Furuta, T., Huber, D., Smear, M. C., Demers, M. and Kleinfeld, D.** (2013). Hierarchy of orofacial rhythms revealed through whisking and breathing. *Nature* **497**, 205–210.
- Muchlinski, M. N.** (2010). A comparative analysis of vibrissa count and infraorbital foramen area in primates and other mammals. *J. Hum. Evol.* **58**, 447–473.
- Neimark, M. A., Andermann, M. L., Hopfield, J. J. and Moore, C. I.** (2003). Vibrissa resonance as a transduction mechanism for tactile encoding. *J. Neurosci.* **23**, 6499–6509.
- Quist, B. W. and Hartmann, M. J. Z.** (2012). Mechanical signals at the base of a rat vibrissa: the effect of intrinsic vibrissa curvature and implications for tactile exploration. *J. Neurophys.* **107**, 2298–2312.
- Quist, B. W., Faruqi, R. A. and Hartmann, M. J. Z.** (2011). Variation in Young's modulus along the length of a rat vibrissa. *J. Biomech.* **44**, 2775–2781.
- Quist, B. W., Seghete, V., Huet, L. A., Murphey, T. D. and Hartmann, M. J. Z.** (2014). Modeling forces and moments at the base of a rat vibrissa during noncontact whisking and whisking against an object. *J. Neurosci.* **34**, 9828–9844.
- Reep, R. L., Gaspard, J. C., III, Sarko, D., Rice, F. L., Mann, D. A. and Bauer, G. B.** (2011). Manatee vibrissae: evidence for a 'lateral line' function. In *New Perspectives on Neurobehavioral Evolution, Annals of the New York Academy of Sciences*, Vol. 1225 (ed. J. I. Johnson, H. P. Zeigler, P. R. Hof), pp. 101–109. Malden: Wiley.
- Reidenbach, M. A. and Koehl, M. A. R.** (2011). The spatial and temporal patterns of odors sampled by lobsters and crabs in a turbulent plume. *J. Exp. Biol.* **214**, 3138–3153.
- Ritt, J. T., Andermann, M. L. and Moore, C. I.** (2008). Embodied information processing: vibrissa mechanics and texture features shape micromotions in actively sensing rats. *Neuron* **57**, 599–613.
- Schooley, R. L. and Branch, L. C.** (2005). Limited perceptual range and anemotaxis in marsh rice rats *Oryzomys palustris*. *Acta Theriol.* **50**, 59–66.
- Shimozawa, T., Murakami, J. and Kumagai, T.** (2003). Cricket wind receptors: thermal noise for the highest sensitivity known. In *Sensors and Sensing in Biology and Engineering* (ed. F. G. Barth, J. A. C. Humphrey, T. W. Secomb), pp. 145–157. New York: Springer-Verlag Wien.
- Solomon, J. H. and Hartmann, M. J. Z.** (2008). Artificial whiskers suitable for array implementation: accounting for lateral slip and surface friction. *IEEE Trans. Rob.* **24**, 1157–1167.
- Solomon, J. H. and Hartmann, M. J. Z.** (2010). Extracting object contours with the sweep of a robotic whisker using torque information. *Intl. J. Rob. Res.* **29**, 1233–1245.
- Towal, R. B., Quist, B. W., Gopal, V., Solomon, J. H. and Hartmann, M. J. Z.** (2011). The morphology of the rat vibrissal array: a model for quantifying spatiotemporal patterns of whisker–object contact. *PLoS Comput. Biol.* **7**, e1001120.
- Welker, W. I.** (1964). Analysis of sniffing of the albino rat. *Behaviour* **22**, 223–244.
- Wieskotten, S., Mauck, B., Miersch, L., Dehnhardt, G. and Hanke, W.** (2011). Hydrodynamic discrimination of wakes caused by objects of different size or shape in a harbour seal (*Phoca vitulina*). *J. Exp. Biol.* **214**, 1922–1930.
- Williams, C. M. and Kramer, E. M.** (2010). The advantages of a tapered whisker. *PLoS ONE* **5**, e8806.
- Wolfe, J., Hill, D. N., Pahlavan, S., Drew, P. J., Kleinfeld, D. and Feldman, D. E.** (2008). Texture coding in the rat whisker system: slip-stick versus differential resonance. *PLoS Biol.* **6**, e215.
- Yan, W., Kan, Q., Kergrene, K., Kang, G., Feng, X.-Q. and Rajan, R.** (2013). A truncated conical beam model for analysis of the vibration of rat whiskers. *J. Biomech.* **46**, 1987–1995.